Modeling sea ice production and dense shelf water formation in coastal polynyas around East Antarctica

Kazuya Kusahara,[1] Hiroyasu Hasumi,[1] and Takeshi Tamura[2]

Received 19 January 2010; revised 26 May 2010; accepted 17 June 2010; published 2 October 2010.

[1] Using an ice-ocean coupled model with fine horizontal resolution around East Antarctica, sea ice production and dense shelf water (DSW) formation in coastal polynyas are investigated. The model reproduces well the locations of coastal polynyas and the high sea ice production there. DSW is formed over the continental shelves under a number of coastal polynyas. A threshold density, beyond which net production of DSW takes place, is largely different among coastal polynyas. The densest and most vigorous DSW formation occurs in the Cape Darnley and Mertz-Ninnis Glacier polynyas followed by somewhat less but still significant DSW formation in the Prydz-Barrier and Vincennes polynyas. Assuming mixing of the DSW outflowing across the shelf break with typical Modified Circumpolar Deep Water over the continental slope, the maximum possible formation rate of Antarctic Bottom Water (AABW) is estimated to be 7.58 Sv around East Antarctica between 60°E and 150°E, with the Cape Darnley and Mertz-Ninnis Glacier polynyas exhibiting the most active formation rates of 2.13 and 1.97 Sv, respectively. From a series of numerical experiments, it is found that the treatment of coastline and grounded icebergs has a large impact on both sea ice production and formation of DSW and AABW.

Citation: Kusahara, K., H. Hasumi, and T. Tamura (2010), Modeling sea ice production and dense shelf water formation in coastal polynyas around East Antarctica, *J. Geophys. Res.*, *115*, C10006, doi:10.1029/2010JC006133.

1. Introduction

[2] Coastal polynyas are areas of open water or newly formed thin ice surrounded by coastline and consolidated thick ice, which are formed by winds and/or oceanic currents during the freezing period, and whose horizontal scale ranges from a few to 100 km [*Pease*, 1987; *Smith et al.*, 1990; *Morales Maqueda et al.*, 2004]. In coastal polynyas, large heat loss occurs due to the direct contact of open water/thin ice with colder air. As a result of the large heat loss, coastal polynyas exhibit high sea ice production rates. Along with sea ice formation, brine rejection occurs and leads to densification of water under coastal polynyas. The modified water over the continental shelf is often called dense shelf water (DSW). Around Antarctica, many coastal polynyas are identified from satellite remote sensing [*Massom et al.*, 1998; *Arrigo and van Dijken*, 2003; *Tamura et al.*, 2007, 2008]. DSW formed in the coastal polynyas plays an important role in the formation of Antarctic Bottom Water (AABW) and thus is linked to the global thermohaline circulation.

[3] Direct sea ice/oceanic measurement in coastal polynyas around Antarctica is temporally and spatially scarce due to logistical difficulties in association with harsh climate conditions. Limited oceanic observations suggest that the variation of DSW in coastal polynyas affects the characteristics of bottom and intermediate waters in the Southern Ocean [*Rintoul*, 2007; *Orsi and Wiederwohl*, 2009]. Numerical modeling in which processes in coastal polynyas are well simulated would facilitate our understanding of variations in the Southern Ocean. In the previous general circulation models with low horizontal resolution, it has been difficult to explicitly capture coastal polynyas and their impacts on the ocean due to their small areal extent [*Stössel and Markus*, 2004; *Wu et al.*, 2003]. *Marsland et al.* [2004] focused on the Mertz Glacier polynya, which is known as one of the source regions for AABW, and investigated sea ice processes and the DSW formation with an ice-ocean coupled model in which a regionally stretched horizontal grid gives fine resolution over the Mertz Glacier polynya.

[4] *Tamura et al.* [2008] derived sea ice production in coastal polynyas all around the Antarctic continent from satellite data and heat flux calculation for the first time. Their result suggests that DSW is formed in several coastal polynyas. The purpose of this study is to realistically reproduce high sea ice formation in coastal polynyas with an ice-ocean coupled model and to investigate its impact on the ocean through the DSW formation. Based on the DSW formation in the model, we also discuss the maximum possible formation rate of AABW in coastal polynyas. We focus on East Antarctica where most of the

[1] Atmosphere and Ocean Research Institute, University of Tokyo, Chiba, Japan.
[2] Antarctic Climate and Ecosystems Cooperative Research Centre, University of Tasmania, Hobart, Tasmania, Australia.

0148-0227/10/2010JC006133

major Antarctic coastal polynyas outside the Weddell and Ross Sea exist.

2. Numerical Model and Experiments

2.1. Coupled Ice-Ocean General Circulation Model

[5] We use an ice-ocean coupled model, named COCO [*Hasumi*, 2006]. The sea ice model adopts a two-category thickness representation. Its thermodynamics is based on *Bitz and Lipscomb* [1999], with one layer for ice and a no heat capacity layer for snow. Prognostic equations for momentum, mass and concentration are taken from *Mellor and Kantha* [1989]. Internal ice stress is formulated by the elastic-viscous-plastic rheology [*Hunke and Dukowicz*, 1997].

[6] The model domain is global. To realize high resolution in the focal region, the two singular points of the horizontal curvilinear coordinate are placed on East Antarctica (70°E 70.5°S and 143°E 68°S). The horizontal grid size over the coastal area in East Antarctica is between a few kilometers and 15 km. The vertical coordinate system of the ocean model is a hybrid of σ (normalized depth) and z. There are 32 vertical levels; σ coordinate is applied to the uppermost five grid points between the free surface and 50 m below the mean surface level, and z coordinate is applied below. The vertical spacing is 5, 5, 8, 12, 20, 30, 40, 50, 60, 70, 80, 90, 100, 110, 120, 130, 140, 150, 180, 200, 200, 200, 300, 300, 300, 400, 400, 400, 400, 500, and 500 m from top to bottom. The partial step representation is adopted for bottom topography [*Adcroft et al.*, 1997].

[7] The ocean model includes the uniformly third-order polynomial interpolation algorithm for tracer advection [*Leonard et al.*, 1993], isopycnal diffusion, isopycnal layer thickness diffusion [*Gent et al.*, 1995], and a surface mixed layer parameterization based on turbulence closure [*Noh and Kim*, 1999]. The isopycnal diffusion coefficient is 1.0×10^2 m^2 s^{-1} and the thickness diffusion coefficient is 1.0 m^2 s^{-1}. The background vertical diffusion coefficient is 1.3×10^{-5} m^2 s^{-1} at the surface and gradually increases up to 2.9×10^{-4} m^{2}s^{-1} with depth (case III of *Tsujino et al.* [2000]). The background vertical viscosity coefficient is 1.0×10^{-4} m^{2}s^{-1}. Horizontal eddy viscosity is parameterized by a Laplacian form, and its coefficient spatially varies so as to resolve the Munk layer. The bottom friction is parameterized by a simple quadratic law with a constant drag coefficient of 1.3×10^{-3}. Convection is represented by a simple convective adjustment scheme.

[8] The ice-ocean drag coefficient is 3.0×10^{-3}, and the turning angle for ice-ocean drag is −10° relative to the direction of the uppermost layer velocity in the ocean model. To parameterize subgrid-scale leads, the maximum sea ice concentration is set 0.98. Salinity of sea ice is fixed at 5 practical salinity units (psu).

[9] In the framework of a two-category sea ice model, the open/newly formed ice area and the consolidated sea ice area coexist in one grid, and a minimum thickness of the consolidated sea ice (demarcation thickness) must be specified. We use the demarcation thickness of 10 cm in this study. This value is consistent with an observational finding that young ice thermodynamically grows to 10 cm thick in open water before thickened by dynamical processes [*Toyota et al.*, 2007].

[10] Model bathymetry and coastline in East Antarctica are shown in Figure 1a. The bathymetry is derived from GEBCO [*Jones et al.*, 1994] and the data around the Adélie Sill (142.0°E–145.0°E, 66.2°S–65.7°S) are modified by recent ship track data [*Porter-Smith*, 2003]. To realistically reproduce the horizontal topographical features, the coastline around Antarctica is modified by ice shelf and iceberg tongue edges identified by MODIS Mosaic of Antarctica Image Map [*Haran et al.*, 2005].

[11] Surface boundary conditions for the model are wind stress, wind speed, air temperature, specific humidity, downward shortwave radiation, downward longwave radiation, fresh water flux, and sea level air pressure. When the surface air temperature is below 0°C, precipitation is treated as snow. Outside of the area within 100 km from the coast of East Antarctica between 50°E and 160°E, sea surface salinity is restored to monthly mean climatology with a 10 day damping time scale 4 to suppress biases of deep convection in offshore region. To calculate wind stress and sensible and latent heat fluxes, we use the bulk formula of *Kara* [2000]. In the northern hemisphere, temperature and salinity are restored to monthly mean climatology [*Steele et al.*, 2001] throughout the water column. After an 18 year integration with the daily surface air climatology of *Röske* [2006], a quasi steady state is obtained. Initiated by this state, we perform a simulation for the period from 1990 to 2007 with surface boundary conditions calculated from daily NCEP-NCAR reanalysis [*Kalnay*, 1996]. The model results for the last 16 years (1992–2007) are utilized for the following analysis. We use monthly and daily averaged values for oceanic and sea ice variables, respectively. In some of the analyses for the ocean, we use monthly climatology during the above period.

2.2. Blocking of Sea Ice Advection by Grounded Icebergs

[12] Observations indicate that coastal polynyas are also formed at the downwind/downstream side of grounded icebergs, as well as along coastlines and floating ice tongues [*Massom et al.*, 1998]. To incorporate blocking of sea ice advection by such grounded icebergs into the model, we prescribe the grid points of grounded icebergs where sea ice velocity is set to zero. It should be noted that oceanic flows are permitted below these grid points. This effect is tested at the Cape Darnley polynya, the Mertz Glacier polynya, and the Ninnis Glacier polynya (see Figure 2 for the location of grounded icebergs). The experiment including this blocking effect is the control case (CTRL).

[13] To investigate impacts of the blocking effect on sea ice and oceanic fields, two additional numerical experiments are performed. One is an experiment without the blocking (NO-GIB), and the other is an experiment where the grid points of grounded icebergs are treated as land points which block ocean flows (LAND).

3. Results of Control Case

3.1. Sea Ice Production, Sea Ice Fields Around Grounded Icebergs, and Oceanic Bottom Density

[14] Spatial distributions of cumulative sea ice production in the model and that estimated from satellite data and heat flux calculation are shown in Figures 1b and 1c, respectively.

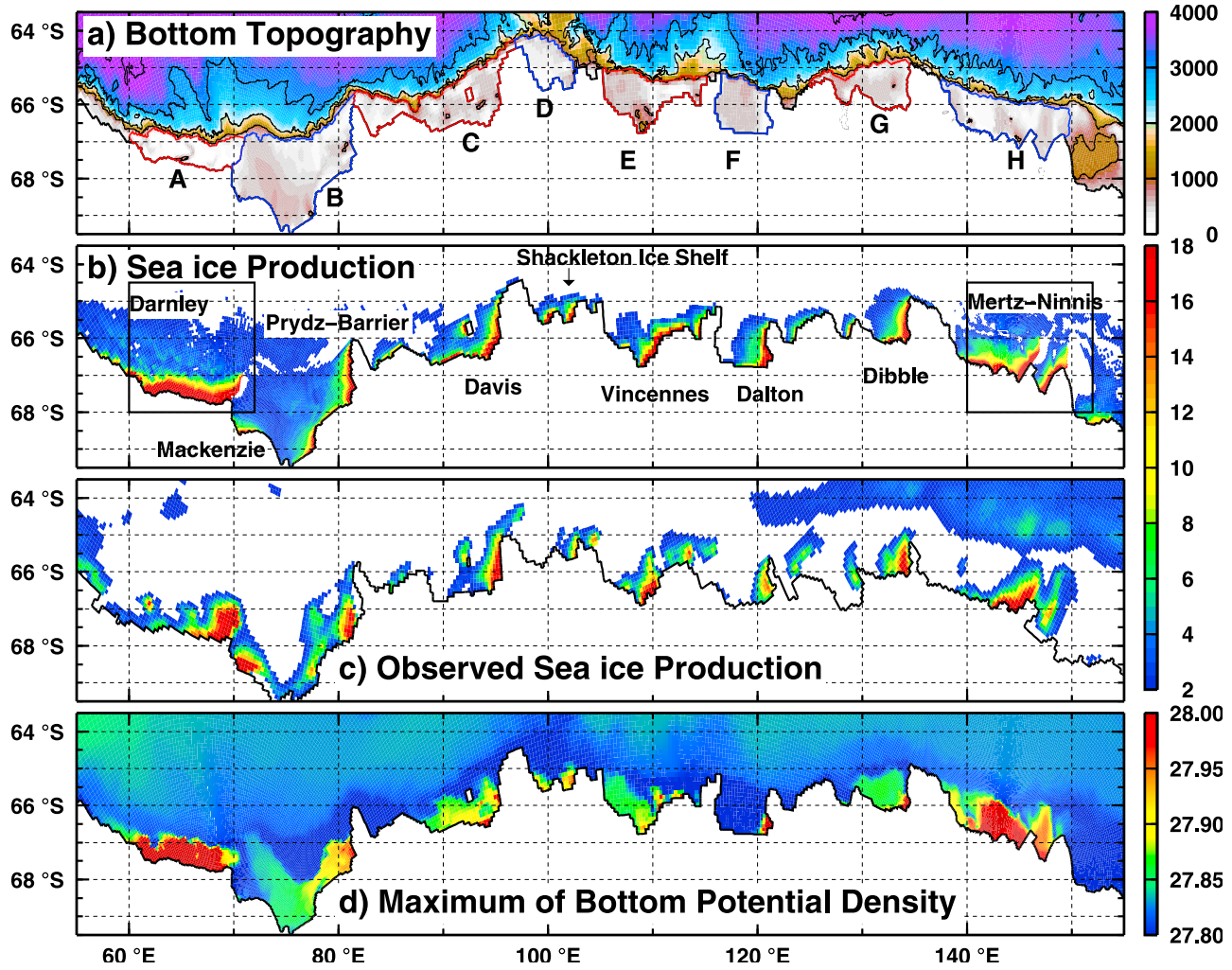

Figure 1. (a) Bottom topography of the model in East Antarctica (m) and control volumes used for the calculation of sea ice production (A–H, red and blue bounded regions). Spatial distribution of (b) cumulative sea ice production in the model (m/yr) and (c) that estimated from satellite data and heat flux calculation [*Tamura et al.*, 2008]. Area of cumulative sea ice production smaller than 2 m is masked out. The names of major coastal polynyas are shown in Figure 1b. (d) Spatial distribution of seasonal maximum potential density at bottom (σ_θ, kg m^{-3}). Squares in Figure 1b show the areas for Figure 2.

For convenience, we use "observation" to mean "satellite-based estimate" in this section. The cumulative sea ice production is calculated by the sum of sea ice production between March and October both for the model result and the observation [*Tamura et al.*, 2008]. Note that a contribution of sea ice melting is not taken into account for the calculation of the cumulative sea ice production, and that the sea ice production is calculated by its daily averages.

[15] A number of patches of high sea ice production are found along the coastline over East Antarctica (Figure 1b). Coastal polynyas are formed on the western (downwind/downstream) side of protruding features, as recognized in satellite data [*Massom et al.*, 1998; *Arrigo and van Dijken*, 2003; *Tamura et al.*, 2007, 2008]. Generally, the model reproduces the locations of coastal polynyas around East Antarctica well.

[16] However, there are four notable differences between the model and observational results. First, the high ice production area around Cape Darnley in the model is wider than in the observation. This is partly explained by the absence of landfast ice in the western part of the area in the model. The landfast ice exhibits a seasonal cycle of the extent with a maximum in winter, which is not reflected in MODIS. The landfast ice blocks sea ice advection and modifies the shape of coastal polynyas. Second, the region of high sea ice production on the western side of grounded icebergs in the Cape Darnley polynya (69°E, 67.3°S) does not extend sufficiently to the west in the model. In reality, small icebergs ground there, and secondary coastal polynyas are considered to be formed on the western side of grounded icebergs. Third, the Mackenzie polynya (70°E, 68.5°S) in the model is much smaller than in the observation. In the model, sub-ice-shelf processes are not incorporated and areas of ice shelves are treated as land grid points. In reality, however, there are oceanic flows under the ice shelves. This size difference suggests that oceanic surface currents from the Amery Ice Shelf could be linked to the formation of the coastal polynya just off the ice shelf. Fourth, sea ice

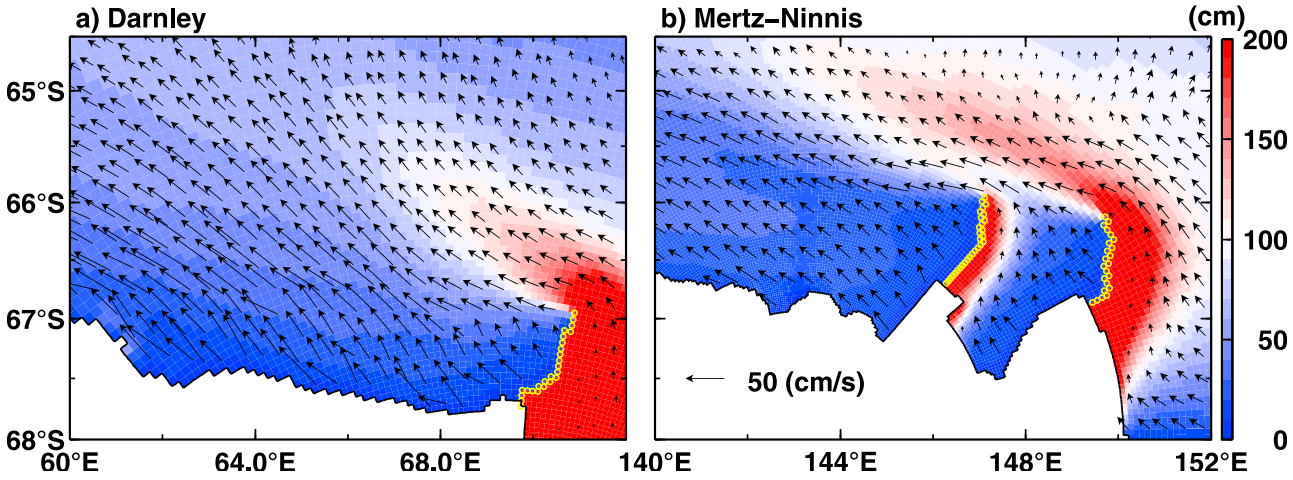

Figure 2. Spatial distribution of monthly averaged sea ice thickness (colors) and sea ice velocity (vectors) for August 1998 in (a) the Cape Darnley polynya and (b) the Mertz-Ninnis Glacier polynyas. Some vectors are thinned out to distinguish them, and yellow open circles show the locations of grounded icebergs.

production in offshore area is larger than in the observation, i.e., blue areas in Figure 1b are larger than in Figure 1c. A possible reason for this difference is described below.

[17] Annual net and cumulative sea ice productions in each polynya are shown in Table 1. All of the control volumes show positive annual net sea ice growth, indicating that these coastal polynyas are effective formation areas of sea ice. The cumulative sea ice production in the model is larger than in the observation. The observed sea ice production, estimated by the method of *Tamura et al.* [2008], has a ±25% uncertainty in the absolute value due mainly to an error (standard deviation) of ±5 cm in estimating thin ice thickness. Their algorithm is tuned for thin ice areas (<20 cm) and the observational sea ice production is counted only when the sea ice thickness is smaller than 20 cm. In the offshore area sea ice thickness is typically 1 m and sometimes thin ice areas are formed by the divergent ice field due to atmospheric synoptic disturbances. Therefore, the sea ice production in the offshore area tends to be conservative estimate and there is large uncertainty in thick ice area. Taking account of these circumstances, the modeled cumulative sea ice production in each coastal polynya is in reasonable agreement with the observation.

[18] Figure 2 shows average sea ice thickness and sea ice velocity fields around the Cape Darnley polynya and the Mertz-Ninnis Glacier polynyas. In these regions, the blocking effect of sea ice advection by grounded icebergs is incorporated into the model. On the eastern side of grounded icebergs or coastline, stagnant sea ice thicker than 2 m exists. Sea ice tongues extend from the northern side of the line of grounded icebergs. On the western side of grounded icebergs or coastline, areas in which sea ice is thinner than 50 cm with a divergent velocity field are formed. In the Mertz Glacier polynya, the modeled characteristics of sea ice fields agree with those of observation [*Massom et al.*, 1998, 2001] and a previous model study [*Marsland et al.*, 2004].

[19] To investigate impacts of coastal polynyas on oceanic water property, a spatial distribution of the seasonal maximum potential density (σ_θ) at bottom, calculated from the modeled monthly climatology, is shown in Figure 1d. Waters whose densities are significantly higher than those offshore are found under the coastal polynyas. These results suggest that dense waters formed under coastal polynyas have a potential to be sources of AABW in the deep ocean. Relatively dense waters are found in the Cape Darnley and Mertz-Ninnis regions.

3.2. Dense Shelf Water Formation

[20] In this section, we focus on water mass exchanges between the continental shelves and the open ocean across shelf breaks. To estimate formation rates of DSW in coastal polynyas, we define control volumes (A–H in Figure 1a) that enclose high sea ice production in coastal polynyas over East Antarctica. To define these control volumes, we use the 500 m depth contours as the offshore boundary because the contours trace shelf breaks well. Deeper depth contours, up to 1000 m, are also used where the 500 m depth contours do not represent shelf breaks well. We use a "threshold density" (σ_{th}) beyond which net production of dense water (positive water mass conversion) takes place in each control volume.

Table 1. Mean and Standard Deviation of Sea Ice Production for Major Coastal Polynyas in East Antarctica[a]

Control Volume	Polynya	Net	Cumulative	Observation
A	Darnley	534.2 ± 57.4	542.9 ± 49.4	300.4 ± 30.9
B	Prydz-Barrier	386.8 ± 49.6	460.0 ± 34.1	457.3 ± 51.8
C	Davis	273.1 ± 44.1	316.5 ± 39.0	245.4 ± 42.5
D	Shackleton Ice Shelf	60.6 ± 26.1	91.6 ± 19.4	60.9 ± 19.0
E	Vincennes	209.8 ± 51.5	243.1 ± 45.7	209.2 ± 31.2
F	Dalton	108.8 ± 34.3	158.1 ± 30.4	100.1 ± 18.4
G	Dibble	189.7 ± 44.6	204.2 ± 42.1	197.7 ± 18.9
H	Mertz-Ninnis	384.6 ± 51.6	424.3 ± 49.9	366.4 ± 38.3

[a]Units are given in km^3. The names of control volumes and coastal polynyas are shown in Figure 1. The cumulative sea ice production is the sum of positive sea ice production between March and October both for the model result and the observation [*Tamura et al.*, 2008]. The net sea ice production is the sum of sea ice production through the year including sea ice melting.

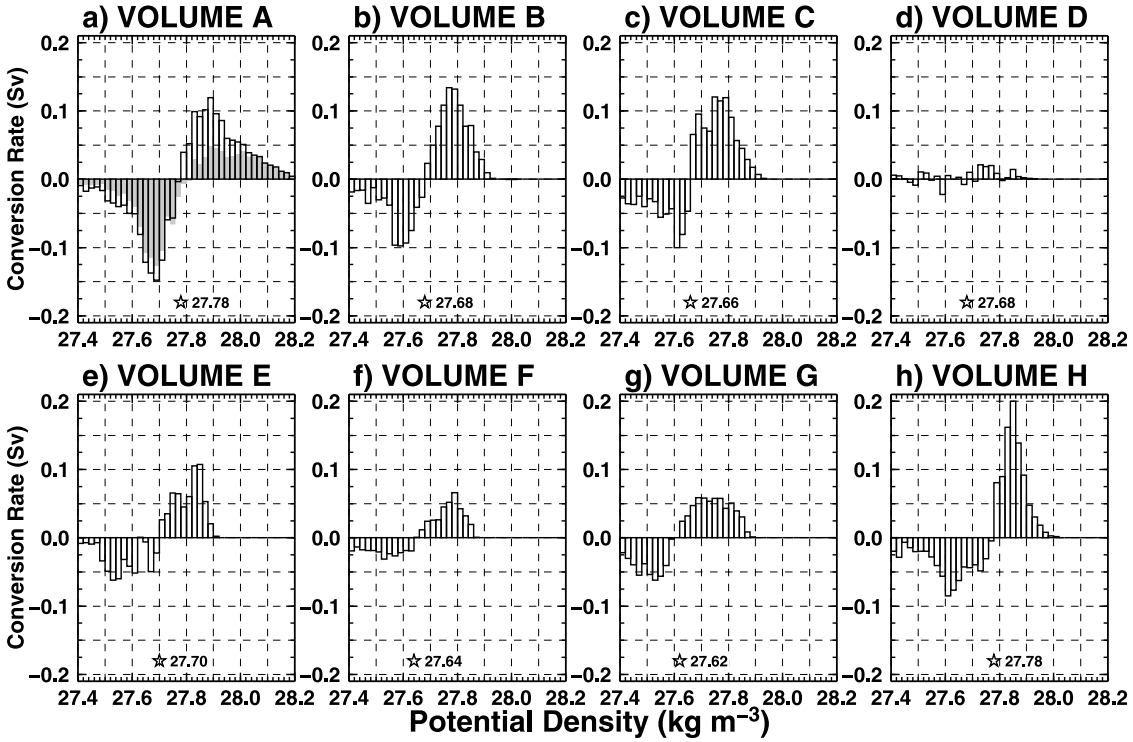

Figure 3. Conversion rate (Sv) of water in the control volumes. The name and location of the control volumes are indicated in Figure 1. Star in each panel shows the threshold density in the control volume. Gray bars in Figure 3a show the transport across the northern boundary of the control volume A.

To estimate the threshold density, we calculate a conversion rate for each potential density bin of 0.02 kgm^{-3} interval. The conversion rate is net volume flux within each density bin across boundaries. It should be noted that volume flux of dense water between two adjacent control volumes (e.g., the control volumes A and B) is negligible. The conversion rate is calculated for each year, and its mean is shown in Figure 3. The threshold density is estimated from the mean conversion rate. Table 2a shows the threshold density, formation rate (with the standard deviation of interannual variations), and mean density of the outflowing DSW for each control volume. The formation rate is the sum of the conversion rates of waters denser than the corresponding threshold density in each control volume.

[21] The threshold density of DSW is largely different among coastal polynyas (Table 2a and Figure 3). In the control volumes A and H, the threshold densities are relatively high (σ_{th} = 27.78 kg m^{-3}), and the DSW formation rates are 1.11 and 0.87 Sv, respectively. There are significantly larger DSW formation rates with relatively high-threshold density in the control volumes E (σ_{th} = 27.70 kg m^{-3}, 0.59 Sv), B (σ_{th} = 27.68 kg m^{-3}, 0.87 Sv), and C (σ_{th} = 27.66 kg m^{-3}, 0.91 Sv). In the control volume D, there is no conversion rate (the threshold is not clear) or DSW formation rate (the mean value and standard deviation of the formation rate are of a comparable magnitude). In the control volumes F and G, the threshold densities are relatively low. The highest DSW mean density is found in the control volume A (σ_θ = 27.933 kg m^{-3}), and the second highest one in the control volume H (σ_θ = 27.854 kg m^{-3}). It should be noted that only 0.55 Sv of DSW outflows across the northern boundary for the control volume A. The rest of DSW outflows on the continental shelf across the western boundary. The mean density of the northward outflowing DSW from the control volume A is 27.988 kg m^{-3}, which is denser than that calculated by using the outflowing DSW across all other boundaries.

[22] To examine potential temperature-salinity characteristics of waters that are exchanged across shelf breaks, the conversion rate is calculated in the potential temperature-salinity space with bin intervals of 0.1°C and 0.02 psu (Figure 4). In Figure 4, the threshold density in each control volume is superimposed, together with γ^n = 28.00 kg m^{-3} and 28.27 kg m^{-3} surfaces (γ^n: neutral density of *Jackett and McDougall* [1997]) which correspond to the highest density (vertically lower limit) of Antarctic Surface Water

Table 2a. DSW Formation in the CTRL Case[a]

Control Volume	Threshold Density σ_{th} (kg m^{-3})	Formation Rate $\sigma_\theta > \sigma_{th}$ (Sv)	Mean Density of Outflow (kg m^{-3})
A	27.78	1.11 ± 0.19 0.55 ± 0.18 (North)	27.933 27.988 (North)
B	27.68	0.87 ± 0.18	27.789
C	27.66	0.91 ± 0.28	27.765
D	(27.68)	0.10 ± 0.07	27.776
E	27.70	0.59 ± 0.19	27.808
F	27.64	0.35 ± 0.11	27.770
G	27.62	0.56 ± 0.18	27.744
H	27.78	0.87 ± 0.12	27.854

[a]For the control volume A, the formation rate and mean density of DSW across the northern boundary are also listed.

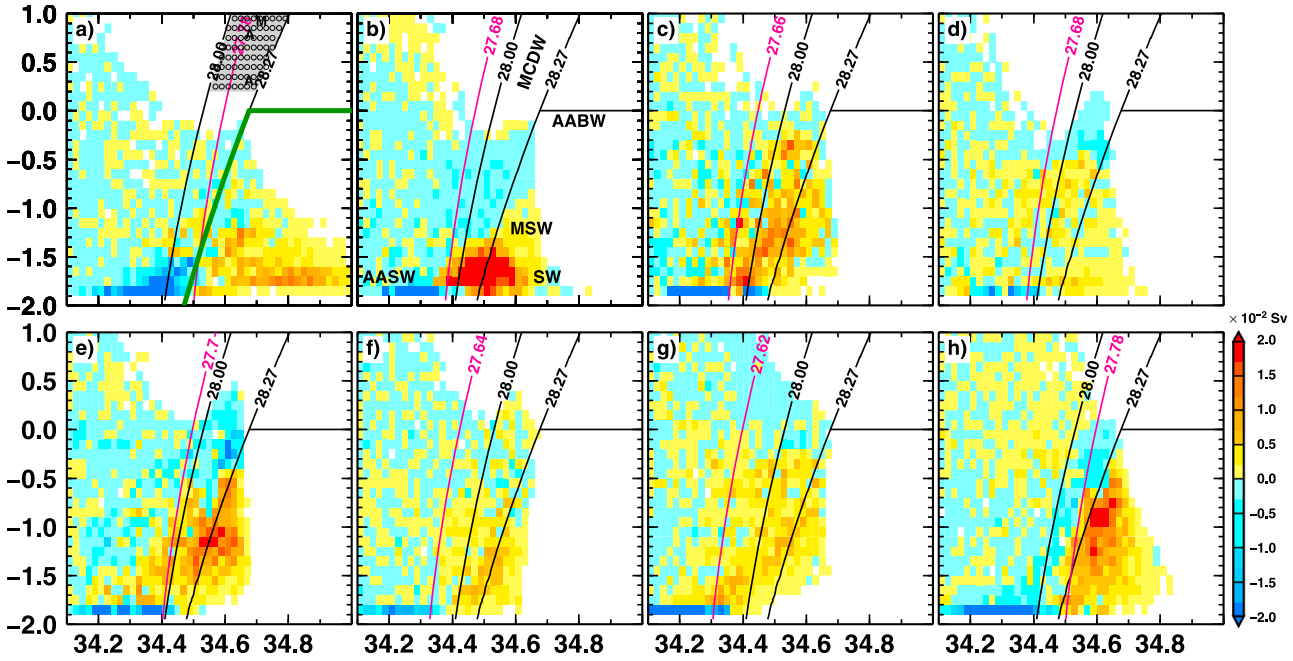

Figure 4. Conversion rate of water in each control volume in the potential temperature-salinity space. Red line shows the threshold potential density (σ_{th}) in the corresponding control volume. Black lines show neutral density of 28.00 kg m^{-3} and 28.27 kg m^{-3} and 0.0°C. Water masses are indicated in Figure 4b. Gray shading with circles in Figure 4a indicates the range of MCDW to be mixed with the outflowing DSW. Labels A and M in Figure 4a show typical water properties of MCDW in the Amery and Mertz regions, respectively. In Figure 4a the transport across the northern boundary is shown.

(AASW) and the lowest density (vertically upper limit) of AABW, respectively [*Orsi et al.*, 1999; *Bindoff et al.*, 2000; *Orsi and Wiederwohl*, 2009]. The layer between the two neutral density surfaces is Modified Circumpolar Deep Water (MCDW). Shelf Water (SW) originates from brine drainage when sea ice is formed and has near freezing temperatures and high salinities. Modified Shelf Water (MSW) is a mixing product of the SW and MCDW penetrating onto the shelf region. These water masses are indicated in Figure 4b.

[23] The dominant component of inflows is near freezing AASW for all control volumes. Potential temperature-salinity characteristics of the outflowing DSW differ significantly from one location to another. In the control volume A, the main component of the outflowing DSW is SW. In the control volume B, the center of the outflowing DSW (34.5 psu, −1.7°C) corresponds to near freezing MCDW and SW. In the control volume C, the outflowing DSW is distributed over MCDW from freezing temperatures to −0.5°C. In the control volume D, there is no significant outflow of DSW. In the control volume E, the center of the outflowing DSW is around salinity of 34.55 psu and potential temperature of −1.2°C, and the outflow takes place along the γ^n = 28.27 kg m^{-3} surface from freezing temperatures to −0.5°C. In the control volumes F and G, the magnitude of outflow is small, although the outflowing DSW is found on the water type corresponding to MCDW. In the control volume H, the center of the outflowing DSW has salinity of 34.6 psu and potential temperature of −0.8°C and ranges over MSW.

[24] Of the waters outflowing from the control volumes, those which have densities higher than γ^n = 28.27 kg m^{-3} have a potential to be a source of AABW [*Williams and Bindoff*, 2003; *Williams et al.*, 2010]. Significant amounts of such dense water outflow are found in the control volumes A, B, E, and H. Potential temperature-salinity characteristics of these outflows depend strongly on the location. The difference can be expected to influence the density or the formation rate of the resulting AABW.

4. Impacts of Grounded Icebergs on Sea Ice and Oceanic Fields

[25] To investigate impacts of the blocking effect of sea ice advection by grounded icebergs on sea ice and oceanic fields, we compare results among the three experiments (CTRL, NO-GIB, and LAND). In the NO-GIB case, coastal polynyas on the western side of grounded icebergs disappear, and thus the sea ice productions decrease there (cumulative sea ice production, A: 487.3 ± 52.6 km^3, H: 369.8 ± 45.8 km^3). In the LAND case, the sea ice fields and sea ice productions increase slightly with respect to the CTRL case (cumulative sea ice production, A: 550.2 ± 48.1 km^3, H: 451.5 ± 52.8 km^3).

[26] As for the influences on the oceanic fields, we focus on the Mertz-Ninnis region, because the Adélie Depression, which is located in the control volume H, is the only area where there are direct in situ observations in winter [*Bindoff et al.*, 2001; *Williams and Bindoff*, 2003]. Figure 5 shows a spatial distribution of the seasonal maximum potential

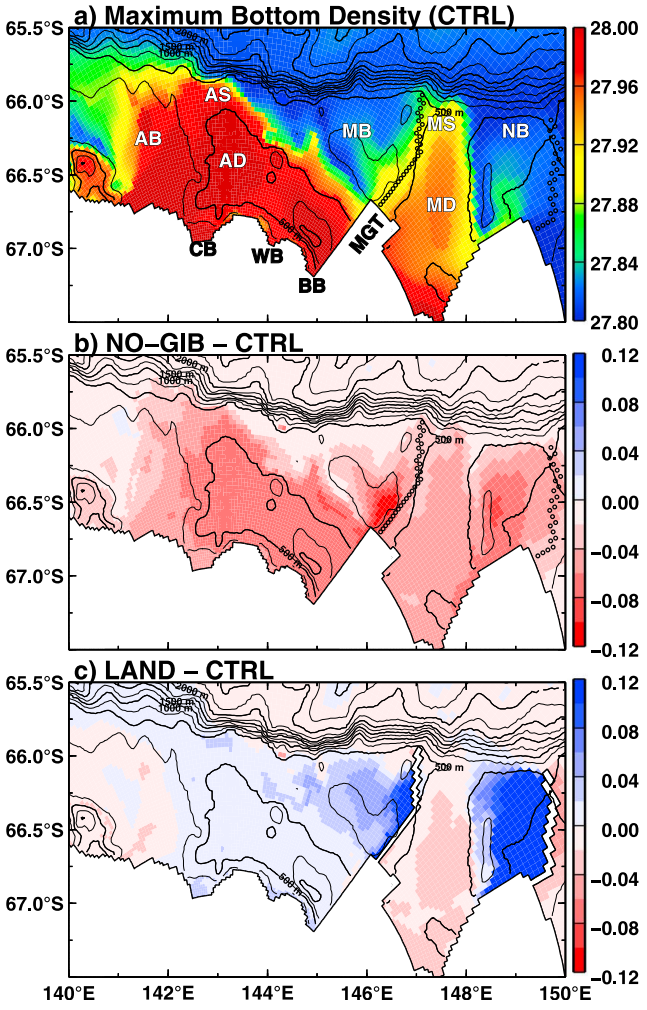

Figure 5. Spatial distribution of (a) seasonal maximum potential density at bottom in the CTRL case and difference of the maximum potential density of the (b) NO-GIB and (c) LAND cases from the CTRL case. Contours indicate depth, and black open circles show the locations of grounded icebergs. Abbreviations of the place names in Figure 5a stand for Adélie Sill (AS), Adélie Depression (AD), Adélie Bank (AB), Mertz Bank (MB), Commonwealth Bay (CB), Buchanan Bay (BB), Watt Bay (WB), Mertz Glacier Tongue (MGT), Mertz Depression (MD), Mertz Sill (MS), and Ninnis Bank (NB).

density at bottom in the CTRL case and those of the difference of the NO-GIB and LAND cases from the CTRL case. Major place names in the control volume H are also shown in Figure 5a. A number of observational studies in the Adélie Depression use a single cutoff potential density of 27.88 kg m^{-3} to separate DSW from MCDW penetrating on the continental shelf [*Bindoff et al.*, 2001; *Williams and Bindoff*, 2003; *Williams et al.*, 2008]. Waters denser than 27.88 kg m^{-3} are considered to be dense enough to sink into the abyssal ocean and to form AABW by being mixed with ambient less dense waters over the continental slope. In the spatial distribution in the CTRL case (Figure 5a), the area of waters denser than 27.88 kg m^{-3} spreads over the Adélie Depression and the Mertz Depression, and the fronts reach the Adélie Sill and the Mertz Sill where outflows of DSW dominantly occur. Additionally, an area of relatively dense water is found near the western side of the grounded icebergs along 147°E. The bottom potential density over the two depressions in the NO-GIB case is lower by approximately 0.07 kg m^{-3} than in the CTRL case (Figure 5b). The difference of bottom potential density in the LAND case is small all over the control volume H, except the western side of the grounded icebergs (Figure 5c).

[27] Figure 6 shows a vertical section of potential density in August in the CTRL case and the difference of the NO-GIB and LAND cases from the CTRL case. The section is parallel to the Mertz Glacier Tongue, from the Mertz Bank to Buchanan Bay. The southern two-thirds of this section is almost identical to an observed section of *Bindoff et al.* [2001] and *Williams and Bindoff* [2003]. In Figure 6a, the sloping isopycnal surfaces indicate that a dense water is formed near the Buchanan Bay. Less dense waters exist to the offshore, wherein a relatively dense water is found on

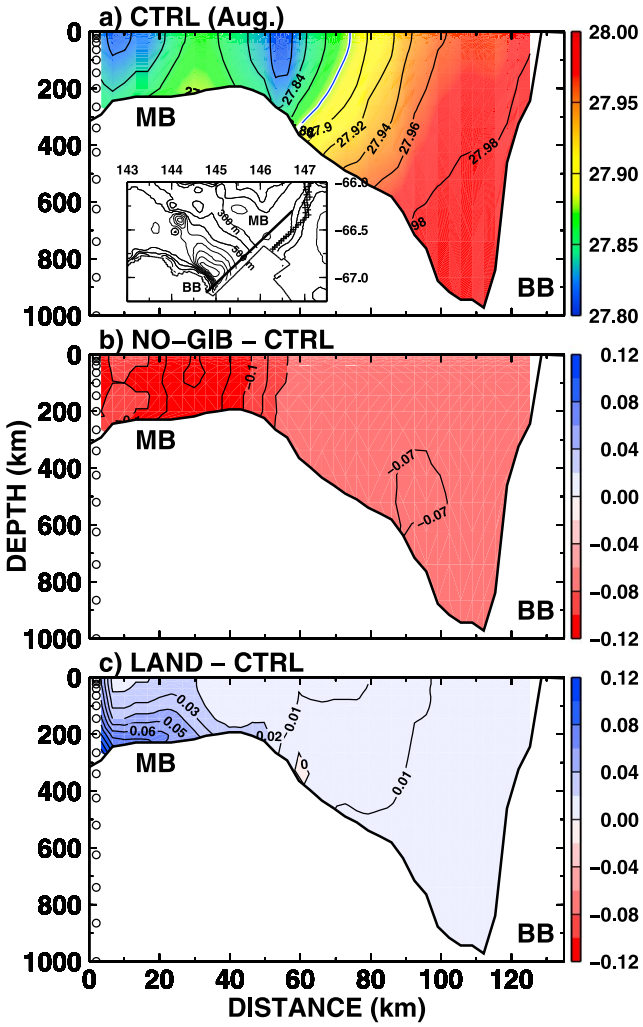

Figure 6. (a) Potential density for the CTRL case and difference of potential density for the (b) NO-GIB and (c) LAND cases from the CTRL case in August along the section shown in the inset of Figure 6a. MB and BB stand for Mertz Bank and Buchanan Bay, respectively. Open circles show the location of the vertical grid cell center points of the model.

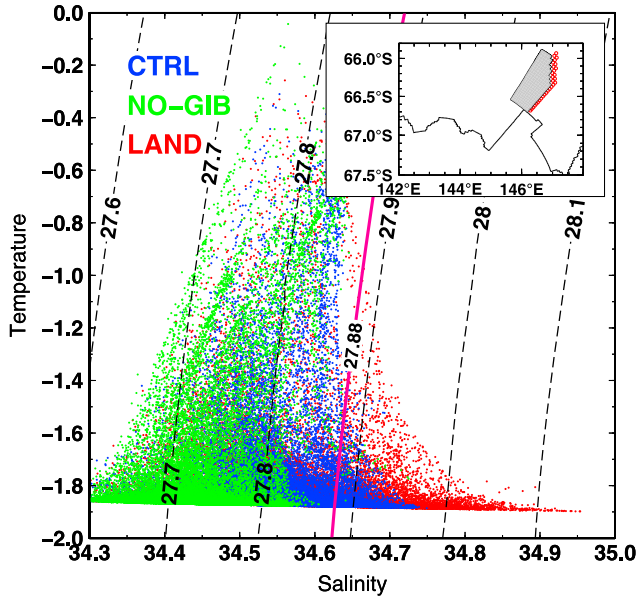

Figure 7. Potential temperature-salinity diagram in the western side of grounded icebergs in the Mertz Glacier polynya in August (gray shading in the inset shows the sampling area). The black contours show the potential density, and a red curve shows thepotential density of 27.88 kg m^{-3}.

the top of the Mertz Bank (Figure 5a). An isopycnal surface of 27.88 kg m^{-3} is located on the southwestern flank of the Mertz Bank in this section and agrees with observational results [*Bindoff et al.*, 2001; *Williams and Bindoff*, 2003]. The potential density along the section in the NO-GIB case is lower everywhere than in the CTRL case. Moreover, there is a large difference of approximately −0.10 kg m^{-3} over the Mertz Bank (Figure 5b), which indicates that the relatively dense water on the Mertz Bank found in the CTRL case is the result of dense water formation along the grounded icebergs. The difference of potential density in the LAND case is small, except near the bottom over the Mertz Bank (Figure 6c). These results indicate that the blocking effect of sea ice by grounded icebergs has its major impact on water masses over the depressions, while their effect on oceanic flows underneath has localized impacts near the grounded icebergs.

[28] To examine differences of water property, we show a potential temperature-salinity diagram of water in August on the western side of grounded icebergs (Figure 7, see the inset for the location). In the NO-GIB case, water denser than 27.88 kg m^{-3} does not exist in accordance with the absence of the coastal polynya on the western side of grounded icebergs. In the CTRL and LAND cases, the water denser than 27.88 kg m^{-3} is formed. However, the water in the LAND case is much denser than in the CTRL case, owing to higher salinity in the LAND case. Maximum salinity in the CTRL case is close to that observed in the Mertz Glacier polynya in winter (about 34.7 psu [*Bindoff et al.*, 2001; *Williams and Bindoff*, 2003]). In the LAND case, mixing of the high-salinity brine with less dense water from the eastern side of grounded icebergs is blocked by the wall of grounded icebergs.

[29] To examine impacts of grounded icebergs on the formation rate of DSW, we calculate the conversion rate in the NO-GIB and LAND cases as well. Figure 8 shows the conversion rates of the three experiments in the control volume H. Conversion rates of the NO-GIB case are significantly reduced in denser classes ($\sigma_\theta \geq 27.82$ kg m^{-3}). In the LAND case, the conversion rates is enhanced in the classes denser than 27.90 kg m^{-3}. The threshold density, the formation rate, and the mean density of the outflowing DSW in the control volume H for the three experiments are shown in Table 2b. The threshold density of the NO-GIB and LAND cases is 27.74 and 27.72 kg m^{-3}, respectively. Although both values are smaller than that of the CTRL case, they are still relatively high compared with the other control volumes.

5. Discussion

5.1. An Estimate of AABW Formation Rate

[30] Potential temperature, salinity, and potential density of the outflowing DSW from the control volumes depend largely on the locations (Figures 3 and 4). Using potential temperature-salinity characteristics of the outflowing DSW, we estimate the maximum possible formation rate of AABW from each control volume. In this estimate, AABW is defined to be water denser than $\gamma^n = 28.27$ kg m^{-3} [*Orsi et al.*, 1999] and lower than 0.0°C in potential temperature. The AABW formation rate is calculated under the following three assumptions. First, we assume that the AABW is a mixing product of the the outflowing DSW (SW or MSW) and MCDW over the continental slope. Second, we assume that MCDW lies between 28.00 kg m^{-3} and 28.27 kg m^{-3} in neutral density and between 0.2°C and 1.0°C in potential

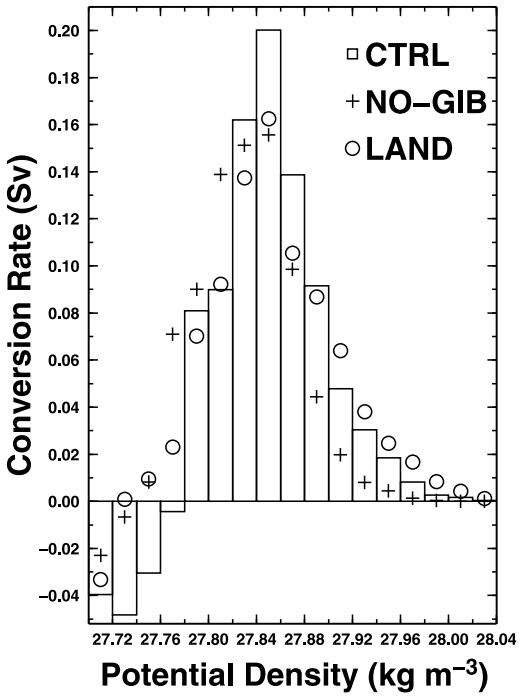

Figure 8. Conversion rate (Sv) of water in the control volume H in the three experiments.

Table 2b. Sensitivity of DSW Formation for the Control Volume H to the Treatment of Grounded Icebergs

Experiment Name	Threshold Density σ_{th} (kg m^{-3})	Formation Rate $\sigma_\theta > \sigma_{th}$ (Sv)	Mean Density of Outflow (kg m^{-3})
CTRL	27.78	0.87 ± 0.12	27.854
NO-GIB	27.74	0.79 ± 0.13	27.832
LAND	27.72	0.85 ± 0.14	27.857

temperature (gray-shaded area in Figure 4a). Labels A and M in Figure 4a show typical water properties of the MCDW in the Amery and Mertz regions, respectively [*Orsi et al.*, 2002]. Third, we assume that all of the outflowing waters denser than γ^n = 28.27 kg m^{-3} and lower than 0.0°C mix with the prescribed MCDW and form uniform AABW of γ^n = 28.27 kg m^{-3}. In other words, the water properties of the estimated AABW is determined by the intersection between the neutral density curve or the potential temperature zero line (green curve in Figure 4a) and the line that connects two water mass characteristics in the potential temperature-salinity space. The mixing ratio of the outflowing DSW to the prescribed MCDW is given by the ratio of distances between the cross point and the source waters in the potential temperature-salinity space.

[31] Table 3 shows the maximum possible formation rates of AABW in each control volume. To show sensitivity to the definition of AABW, the AABW formation rate with γ^n = 28.30 kg m^{-3} is also listed in Table 3. The AABW formation rate is estimated against a number of MCDW samples (67 points in the gray-shaded area in Figure 4a), and the mean and the standard deviation are calculated for each control volume. It should be noted that the AABW formation rate in the control volume A is estimated using the outflowing DSW across the northward boundary. There are active formations of AABW in the control volumes A and H, with formation rates of 2.13 and 1.97 Sv, respectively. The control volumes B and E also show significant formation of 1.29 and 0.93 Sv, respectively. Although the DSW formation rate in the control volume A (0.55 Sv) is smaller than in the control volume H (0.87 Sv), the AABW formation in these control volumes are comparable to each other, because high salinities and low potential temperatures of the outflowing DSW from the control volume A lead to the large mixing ratio of DSW relative to MCDW. The total maximum possible formation rate of AABW is 7.58 Sv around East Antarctica between 60°E and 150°E.

5.2. Impacts of Grounded Icebergs on the AABW Formation Rate

[32] In the NO-GIB case, the AABW formation rates of the control volume A and H are 1.87 ± 0.54 and 1.46 ± 0.48 Sv, respectively, and these rates are smaller than those in the CTRL case. They are 2.14 ± 0.61 and 1.77 ± 0.53 Sv, respectively, in the LAND case. In the control volume A, the AABW formation rate in the LAND case is similar to that in the CTRL case. In the control volume H, the AABW formation rate in the LAND case is smaller by 0.2 Sv than that in the CTRL case. This comes from the decrease of the DSW formation rate and the change of the threshold density (Figure 8 and Table 2b). The AABW formation rate in the experiment without blocking grounded icebergs (NO-GIB case) decreases by 12–26% when compared with the experiments including grounded icebergs (CTRL and LAND cases), suggesting importance of water mass formation on the lee side of the grounded icebergs.

6. Conclusion

[33] Using an ice-ocean coupled model with regionally fine horizontal resolution around East Antarctica, we investigated sea ice production and DSW formation in coastal polynyas. The model which includes the blocking effect of sea ice advection by grounded icebergs reproduces well the locations of coastal polynyas and high sea ice production there, and DSW is found under these coastal polynyas (Figures 1b and 1c and Tables 1 and 2a). From a series of numerical experiments, we demonstrated that a treatment of grounded icebergs has large impacts on the sea ice and ocean fields and the formation rates of DSW and AABW (Figures 5–8 and Table 2b).

[34] The density and potential temperature-salinity characteristics of DSW are largely different among coastal polynyas (Table 2a and Figures 3 and 4). Corresponding to the high sea ice production (Table 2a), high formation rates of the densest DSW are found in the Cape Darnley and Mertz-Ninnis Glacier polynyas (control volumes A and H). Significant formation of relatively dense DSW are also found in the Prydz-Barrier and Vincennes polynyas (control volume B and E). This result suggests that these coastal polynyas are possible source regions for AABW, supporting observational results of dense water formation [*Rintoul*, 1998; *Bindoff et al.*, 2000; *Meijers et al.*, 2010].

[35] We estimate the maximum possible formation rate of AABW by assuming mixing of the outflowing DSW from the continental shelves with typical MCDW over the continental slope. It is found that Cape Darnley and Mertz-Ninnis are significant source regions of AABW with the formation rates of 2.13 and 1.97 Sv, respectively. The total AABW formation rate all around East Antarctica is 7.58 Sv and is comparable to that in the Weddell Sea [*Naveira Garabato et al.*, 2002], indicating the importance of the water mass transformation in coastal polynyas there.

[36] However, it should be noted that only a part of the outflow of DSW would in reality sink to greater depth as a dense water plume tends to flow along an isobath due to the Earth's rotation, and the formation rate of AABW strongly depends on the mixing process of DSW with less dense

Table 3. Maximum Possible Formation Rate of AABW in the Control Volumes A–H

Control Volume	$\gamma^n > 28.27$ & $\theta < 0.0$ (Sv)	$\gamma^n > 28.30$ & $\theta < 0.0$ (Sv)
A	2.13 ± 0.61	1.97 ± 0.51
B	1.29 ± 0.53	1.05 ± 0.32
C	0.59 ± 0.20	0.45 ± 0.11
D	0.18 ± 0.07	0.15 ± 0.05
E	0.93 ± 0.31	0.71 ± 0.17
F	0.27 ± 0.11	0.20 ± 0.05
G	0.22 ± 0.07	0.16 ± 0.03
H	1.97 ± 0.61	1.64 ± 0.41
Total	7.58	6.33

ambient waters over the continental slope. In the present model, due mainly to the coarse vertical resolution, the mixing process over the slope is not reproduced well. To reproduce the formation and the path of AABW, we need a model with much higher resolutions both in the horizontal and vertical directions which explicitly resolves the bottom boundary layer over the steep continental slope around Antarctica.

[37] **Acknowledgments.** We would like to thank G. D. Williams for topography data around the Adélie Sill. Numerical calculations were performed on SR11000 and HA8000 at Information Technology Center, University of Tokyo. This study is supported by JST/CREST.

References

Adcroft, A., C. Hill, and J. Marshall (1997), Representation of topography by shaved cells in a height coordinate ocean model, *Mon. Weather Rev.*, *125*(9), 2293–2315.

Arrigo, K. R., and G. L. van Dijken (2003), Phytoplankton dynamics within 37 Antarctic coastal polynya systems, *J. Geophys. Res.*, *108*(C8), 3271, doi:10.1029/2002JC001739.

Bindoff, N. L., M. A. Rosenberg, and M. J. Warner (2000), On the circulation and water masses over the Antarctic continental slope and rise between 80 and 150°E, *Deep Sea Res., Part II*, *47*, 2299–2326.

Bindoff, N. L., G. D. Williams, and I. Allison (2001), Sea-ice growth and water-mass modification in the Mertz Glacier polynya, East Antarctica, during winter, *Ann. Glaciol.*, *33*, 399–406.

Bitz, C. M., and W. H. Lipscomb (1999), An energy-conserving thermodynamics model of sea ice, *J. Geophys. Res.*, *104*(C7), 15,669–15,677.

Gent, P. R., J. Willbrand, T. J. McDougall, and J. C. McWilliams (1995), Parameterizing eddy-induced tracer transports in ocean circulation models, *J. Phys. Oceanogr.*, *25*, 463–474.

Haran, T., J. Bohlander, T. Scambos, T. Painter, and M. Fahnestock (2005), MODIS Mosaic of Antarctica (MOA) Image Map, http://nsidc.org/data/nsidc-0280.html, Natl. Snow and Ice Data Cent., Boulder, Colo. (Updated 2006.)

Hasumi, H. (2006), CCSR Ocean Component Model (COCO) version 4.0, *Rep. 25*, Cent. for Clim. Syst. Res., Univ. of Tokyo, Chiba, Japan.

Hunke, E. C., and J. K. Dukowicz (1997), An elastic-viscous-plastic model for sea ice dynamics, *J. Phys. Oceanogr.*, *27*, 1849–1867.

Jackett, D. R., and T. J. McDougall (1997), A neutral density variable for the world's oceans, *J. Phys. Oceanogr.*, *27*, 237–263.

Jones, M. T., A. R. Tabor, and P. Weatherall (1994), GEBCO digital atlas: Supporting volume, report, Br. Oceanogr. Data Cent., Birkenhead, U. K.

Kalnay, E. (1996), The NCEP/NCAR 40 year-reanalysis project, *Bull. Am. Meteorol. Soc.*, *77*, 437–470.

Kara, A. B. (2000), Efficient and accurate bulk parameterizations of air-sea fluxes for use in General Circulation Models, *J. Atmos. Oceanic Technol.*, *17*, 1421–1438.

Leonard, B. P., M. K. MacVean, and A. P. Lock (1993), Positivity-preserving numerical schemes for multidimensional advection, *Tech. Memo 106005*, 62 pp., Lewis Res. Cent., NASA, Cleveland, Ohio.

Marsland, S. J., N. L. Bindoff, G. D. Williams, and W. F. Budd (2004), Modeling water mass formation in the Mertz Glacier Polynya and Adélie Depression, East Antarctica, *J. Geophys. Res.*, *109*, C11003, doi:10.1029/2004JC002441.

Massom, R. A., P. T. Harris, K. J. Michael, and M. J. Potter (1998), The distribution and formative processes of latent-heat polynyas in East Antarctica, *Ann. Glaciol.*, *27*, 420–426.

Massom, R. A., K. L. Hill, V. I. Lytle, A. P. Worby, M. J. Paget, and I. Allison (2001), Effects of regional fast-ice and iceberg distributions on the behaviour of the Mertz Glacier polynya, East Antarctica, *Ann. Glaciol.*, *33*, 391–398.

Meijers, A. J. S., A. Klocker, N. L. Bindoff, G. D. Williams, and S. J. Marsland (2010), The circulation and water masses of the Antarctic shelf and continental slope between 30 and 80°E, *Deep Sea Res., Part II*, *57*, 723–737.

Mellor, G. L., and L. Kantha (1989), An ice-ocean coupled model, *J. Geophys. Res.*, *94*(C8), 10,937–10,954.

Morales Maqueda, M. A., A. J. Willmott, and N. R. T. Biggs (2004), Polynya dynamics: A review of observations and modeling, *Rev. Geophys.*, *42*, RG1004, doi:10.1029/2002RG000116.

Naveira Garabato, A. C., E. L. McDonagh, D. P. Stevens, K. J. Heywood, and R. J. Sanders (2002), On the export of Antarctic Bottom Water from the Weddell Sea, *Deep Sea Res., Part II*, *49*, 4715–4742.

Noh, Y., and H. J. Kim (1999), Simulations of temperature and turbulence structure of the oceanic boundary layer with the improved near-surface process, *J. Geophys. Res.*, *104*(C7), 15,621–15,634.

Orsi, A. H., and C. L. Wiederwohl (2009), A recount of Ross Sea waters, *Deep Sea Res., Part II*, *56*, 778–795.

Orsi, A. H., G. C. Johnson, and J. L. Bullister (1999), Circulation, mixing, and production of Antarctic Bottom Water, *Prog. Oceanogr.*, *43*(1), 55–109.

Orsi, A. H., W. M. Smethie Jr., and J. L. Bullister (2002), On the total input of Antarctic waters to the deep ocean: A preliminary estimate from chlorofluorocarbon measurement preliminary estimate from chlorofluorocarbon measurements, *J. Geophys. Res.*, *107*(C8), 3122, doi:10.1029/2001JC000976.

Pease, C. H. (1987), The size of wind-driven coastal polynyas, *J. Geophys. Res.*, *92*(C7), 7049–7059.

Porter-Smith, R. (2003), Bathymetry of the George Vth Land shelf and slope, *Deep Sea Res., Part II*, *50*, 1337–1347.

Rintoul, S. R. (1998), On the origin and influence of Adélie Land Bottom Water, in *Ocean, Ice, and Atmosphere: Interactions at the Antarctic Continental Margin*, *Antarct. Res. Ser.*, vol. 75, edited by S. S. Jacobs and R. F. Weiss, pp. 151–171, AGU, Washington, D. C.

Rintoul, S. R. (2007), Rapid freshening of Antarctic Bottom Water formed in the Indian and Pacific oceans, *Geophys. Res. Lett.*, *34*, L06606, doi:10.1029/2006GL028550.

Röske, F. (2006), A global heat and freshwater forcing dataset for ocean models, *Ocean Modell.*, *11*, 235–297.

Smith, S. D., R. D. Muench, and C. H. Pease (1990), Polynyas and leads: An overview of physical processes and environment, *J. Geophys. Res.*, *95*(C6), 9461–9479.

Steele, M., R. Morley, and W. Ermold (2001), PHC: A global ocean hydrography with a high-quality Arctic Ocean, *J. Clim.*, *14*, 2079–2087.

Stössel, A., and T. Markus (2004), Using satellite-derived ice concentration to represent Antarctic coastal polynyas in ocean climate models, *J. Geophys. Res.*, *109*, C02014, doi:10.1029/2003JC001779.

Tamura, T., K. I. Ohshima, T. Markus, D. J. Cavalieri, S. Nihashi, and N. Hirasawa (2007), Estimation of thin ice thickness and detection of fast ice from SSM/I data in the Antarctic Ocean, *J. Atmos. Oceanic Technol.*, *24*, 1757–1772.

Tamura, T., K. I. Ohshima, and S. Nihashi (2008), Mapping of sea ice production for Antarctic coastal polynyas, *Geophys. Res. Lett.*, *35*, L07606, doi:10.1029/2007GL032903.

Toyota, T., S. Takatsuji, K. Tateyama, K. Naoki, and K. I. Ohshima (2007), Properties of sea ice and overlying snow in the southern Sea of Okhotsk, *J. Oceanogr.*, *63*, 393–411.

Tsujino, H., H. Hasumi, and N. Suginohara (2000), Deep Pacific circulation controlled by vertical diffusivity at the lower thermocline depths, *J. Phys. Oceanogr.*, *30*, 2853–2865.

Williams, G. D., and N. L. Bindoff (2003), Wintertime oceanography of the Adélie Depression, *Deep Sea Res., Part II*, *50*, 1373–1392.

Williams, G. D., N. L. Bindoff, S. J. Marsland, and S. R. Rintoul (2008), Formation and export of dense shelf water from the Adélie Depression, East Antarctica, *J. Geophys. Res.*, *113*, C04039, doi:10.1029/2007JC004346.

Williams, G. D., S. Aoki, S. S. Jacobs, S. R. Rintoul, T. Tamura, and N. L. Bindoff (2010), Antarctic Bottom Water from the Adélie and George V land coast, East Antarctica (140–149°E), *J. Geophys. Res.*, *115*, C04027, doi:10.1029/2009JC005812.

Wu, X., W. F. Budd, and I. Allison (2003), Modelling the impacts of persistent Antarctic polynyas with an atmosphere-sea-ice general circulation model, *Deep Sea Res., Part II*, *50*, 1357–1372.

H. Hasumi and K. Kusahara, Atmosphere and Ocean Research Institute, University of Tokyo, 5-1-5 Kashiwanoha, Kashiwa-shi, Chiba 277-8568, Japan. (kusahara@aori.u-tokyo.ac.jp)

T. Tamura, Antarctic Climate and Ecosystems Cooperative Research Centre, University of Tasmania, Private Bag 80, Hobart, Tasmania 7001, Australia.